 doi:10.20944/preprints202208.0049.v1

Structure and Reactivity of $CoFe_2O_4$ (001)surfaces in Contact with a Thin Water Film

T. Kox[1], A. H. Omranpoor[1] and S. Kenmoe[1]

[1]Department of Theoretical Chemistry, University of Duisburg-Essen, Universitätsstr. 2, D-45141 Essen, Germany
August 1, 2022

Correspondence:stephane.kenmoe@uni-due.de

Abstract

$CoFe_2O_4$ is a promissing catalytic material for many chemical reactions. We have used ab initio molecular dynamic simulations to study the structure and reactivity of the A- and B-terminations of the low index $CoFe_2O_4$ (001) surfaces to water adsorption at room temperature. Upon adsorption, water partly dissociates on both termination with a higher dissociation degree on the A-termination (30% versus 19%). The 2-fold coordinated Fe^{3+}(tet) in the tetrahedral voids and the 5-fold coordinated Fe^{3+}(oct) in the octahedral voids are the main active sites for water dissociation on the A- and B-termination, respectively. Molecular water, hydroxydes and surface OH resulting from proton transfer to surface oxygens are present on the surfaces. Both water free surface terminations undergo reconstruction. The outermost Fe^{3+}(tet) on the A-termination and B-termination move towards the nearby unoccupied octahedral voids. In the presence of a thin film of 32 water molecules, the reconstructions are partially and completely lifted on the A- and B-termination, respectively.

Key words: molecular dynamis; spinels; water adsorption

 doi:10.20944/preprints202208.0049.v1

1 Introduction

Spinel-type transition metal oxides (TMO) are increasingly used as catalysts for the production of chemicals at the industrial level via heterogeneous catalysis. This stems from their interesting electronic, magnetic, optical, electrical, thermal and redox properties.[1] Among these, cobalt ferrite($CoFe_2O_4$) was found to be a promissing catalytic material for many chemical reactions due to its unique structural and chemical stability.[2,3,4] These include the oxygen evolution reaction (OER),[5,6,7,8] CO oxidation,[8,9,10,11,12] 2-propanol oxidation,[13,14], alkene oxidation,[15] methane combution[16] and oxidation of many other organic compounds.[17]

$CoFe_2O_4$ nanoparticules grow naturally as octahedrons exposing only the low index (111) facet. This stems from the surface energy of this facet (0.208 $J.m^{-2}$) which is one order of magnitude lower than the two other low index (001) and (101) facets (1.486 $J.m^{-2}$ and 1.916 $J.m^{-2}$, respectively) as calculated by Zheng et al.[18] Based on these surfaces energies, they computed the equilibrium shape of $CoFe_2O_4$ using a Wulff construction. Their calculations showed octahedral grains exposing 8 (111) facets only, in agreement with scanning electron microscopy (SEM) images observed experimentally.[19]

However in operando, it may happen that less stable facets show better catalytic performance for particular chemical reactions. Control parameters such like the solvent may act as selective surfactants and promote the growth of a particular surface termination.[20] In this respect, the performance the (111) facet for OER has been questioned recently by Hajiyani et al. as a considerable disagreement between the calculated and experimental overpotentials was observed.[21,5,6] Using DFT calculations, they investigated the catalytic performance of pure and chemically modified $CoFe_2O_4$ (001) surfaces for OER and found that this less stable facet shows a lower overpotential.[21]

Besides, several synthesis routes, have been developed in recent years to tune the size, shape and composition of $CoFe_2O_4$ nanoparticules and promote a selective exposure of catalytically relevant facets. Depending on the interplay between the synthesis parameters such as temperature, reaction time and solvent, nanoparticles with various shapes can be synthesized.[22] For exam-

 doi:10.20944/preprints202208.0049.v1

ple, Kim et al. recently proposed a recipe that enables the growth of highly crystalline nanohexagons exposing not only the (111) facets but also the (001) facets in considerable proportions.[23] Apart from temperature and reaction time, ratio of surfactant to solvent was found to be a decisive parameter in their study. Hence, for a rational design and improvement of properties of $CoFe_2O_4$ nanoparticles, the role of the solvent should be elucidated.

Recently a primordial step towards understanding of the effect of aqeous solvation on the properties of $CoFe_2O_4$ nanoparticles was performed by Rushiti et al.[24] They used static DFT calculations to investigate the structure and reactivity of clean and O-defected $CoFe_2O_4$ (001) surface towards water in the single molecule regime. Water was found to adsorb mainly molecularly form on Co and Fe metal sites of defect-free surfaces, whereas it always dissociates at oxygen vacancies, lifting thereby the reconstructions introduced by the defects.

However for processes in operando, the dynamical character of the disordered liquid water phase and the thermal contributions to its structure and reactivity have to be taken into account. In this work, we use ab initio molecular dynamic simulations to shied some light on the structural response and reactivity of $CoFe_2O_4$ (001) surfaces to water adsorption at room temperature. We investigate the nature of the adsorption sites and the chemical state of water in the contact layers. We consider both the so-called A- and B-terminations of $CoFe_2O_4$ (001) and a water film of approximately 2 Å to 3 Å and consisting of 32 water molecules. As shown in previous studies this thickness of interfacial water describes reasonably well the interface between water and many oxides.[20,25,26,27,28]

2 Computational details

Cobalt ferrite ($CoFe_2O_4$) crystallises in a face cubic centred inverse spinel,[2] with an inversion degree that depends on the synthesis conditions. In this work we consider a full inverse spinel structure, where 1/4 of the octahedral voids are co-occupied by cobalt Co^{2+}(oct) and Fe^{3+}(oct), while the tetrahedral voids are occupied only by Fe^{3+}(tet) . We alternate the occupation of the octahedral voids with Co^{2+} and Fe^{3+} with every layer in the x direction (surface in-plane).

Preprints (www.preprints.org) | NOT PEER-REVIEWED | Posted: 2 August 2022 doi:10.20944/preprints202208.0049.v1

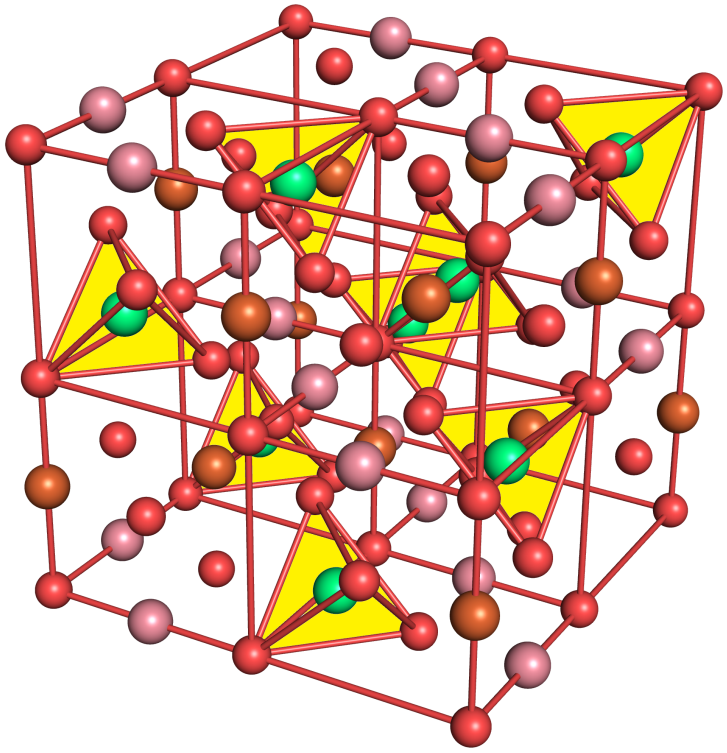

Figure 1: $CoFe_2O_4$ bulk structure. Fe^{3+}(tet) ions in tetrahedral voids (yellow) are shown in green, Fe^{3+}(oct) and Co^{2+}(oct) ions in octahedral voids in brown and purple and oxygen atoms in red.

Cutting in the (001) direction leads to two different surface terminations known as A- and B-terminations (see Figure 2). The topmost layer (L0) of the A-termination shows only 2-fold coordinated Fe^{3+}(tet) ions occupying the tetrahedral voids, while the topmost layer (L1) of the B-termination is mixed, consisting 5-fold coordinated Co^{2+}(oct) and Fe^{3+}(oct) ions which sit in the octahedral voids and surface oxygens.

Preprints (www.preprints.org) | NOT PEER-REVIEWED | Posted: 2 August 2022 doi:10.20944/preprints202208.0049.v1

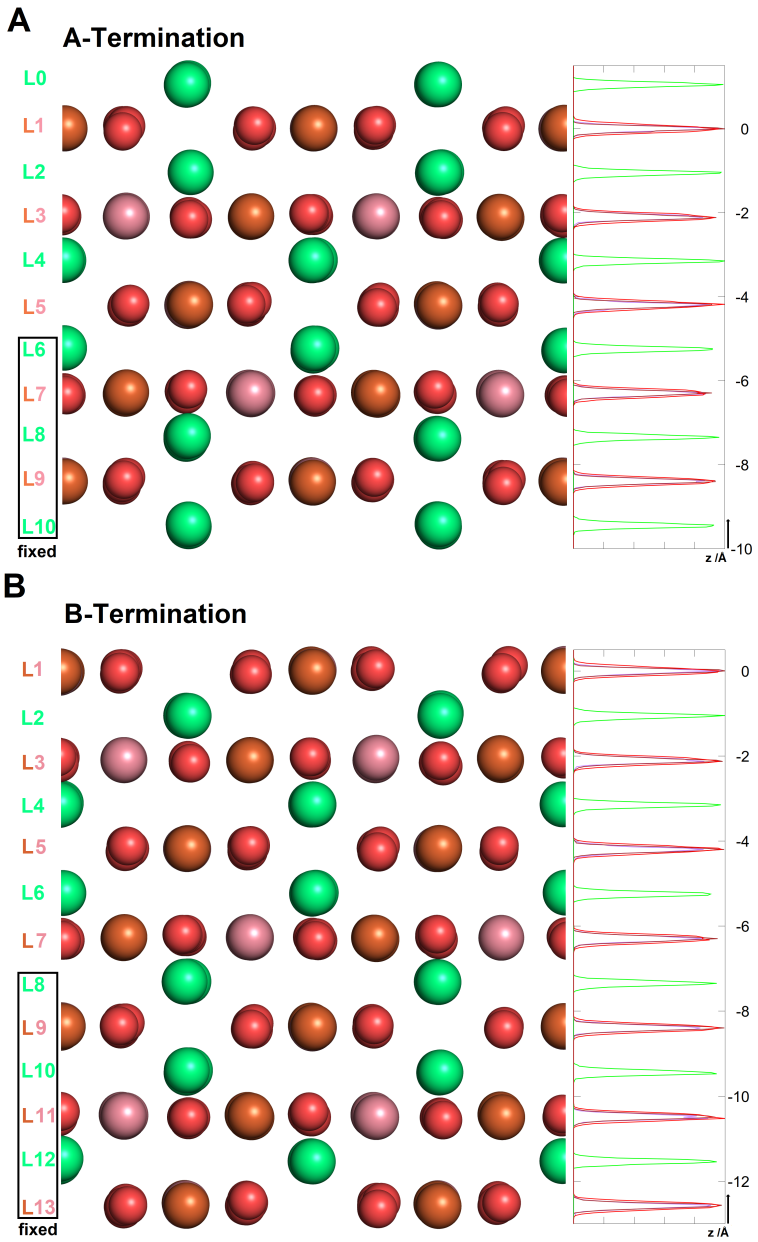

Figure 2: A- (top) and B-terminations (bottom) of the $CoFe_2O_4$ (001) surface. Fe^{3+}(tet) ions in tetrahedral voids are shown in green, Fe^{3+}(oct) and Co^{2+}(oct) ions in octahedral voids in brown and purple and oxygen atoms in red. On the left, various layers are defined, and atom density profiles along the z axis are shown on the right. Layers L6 to L10 and L8 to L13 were kept rigid for A- and B-terminations, respectively.

 doi:10.20944/preprints202208.0049.v1

To model the interaction of the surfaces with the water film, non stoichiometric slabs consisting of 11 and 13 atomic layers covered with a water film of 32 molecules and followed by a vacuum region of about 20 Å thickness were used for A- and B-termination, respectively. In each case, 5 (A-termination) and 6 (B-termination) atomic layers in the bottom part of the slabs were frozen at their bulk positions and the upper part of the slab allowed to relax together with the water molecules. A supercell with (2x2) periodicity in the lateral direction (x and y) and corresponding dimensions of 16.784 Å × 16.784 Å × 40.0 Å was used. A dipole correction was applied in the surface's. out of plane direction to cancel the electric field gradient in the vacuum, arising from the asymmetry of the slabs due to frozen atoms in the bottom part and the one-sided water adsorption.

The CP2K/Quickstep package[29] was used to perform Born-Oppenheimer molecular dynamics (MD) simulations. The electronic interactions were treated with the PBE exchange-correlation functional[30] together with a dispersion correction of the Grimme D3 type.[31] Hubbard correction[32] terms of $U = 2.0$ eV[26,33,34,35] for Co and $U = 3.3$ eV[36] for Fe were added for a correct description of their 3d states. The core electrons were treated with Goedecker-Teter-Hutter (GTH) pseudopotentials, while the 3s, 3p, 3d, and 4s, electrons of Co and Fe atoms and the the 2s and 2p electrons of the O atoms were considered as valence electrons. The basis sets consisted of a mixture of double-ζ quality local basis functions with one set of polarization functions (DZVP) and plane waves with cutoff of 500 Ry.

The Born-Oppenheimer molecular dynamics trajectories were propagated with a time step of 0.5 fs during a total simulation time of 20 ps. To achieve NVT conditions, a Nosé-Hoover thermostat with a time constant of 1 ps and a target temperature of 300 K was used.

Preprints (www.preprints.org) | NOT PEER-REVIEWED | Posted: 2 August 2022 doi:10.20944/preprints202208.0049.v1

3 Results and discussions

3.1 The structure of interfacial water

The A- and B-terminations of $CoFe_2O_4$ (001) surface show open surfaces where water can bind on several potential adsorption sites. These are the 2-fold coordinated Fe^{3+}(tet) , the 5-fold coordinated Co^{2+}(oct) and Fe^{3+}(oct). On both terminations one differentiates between surface oxygens O1 in the topmost layer (L1) that are bound to one Fe^{3+}(tet) in the nearest subsurface layer L2 and those that are not (O2). To investigate the adsorption mode of water at the interface, we have calculated characteristic radial distribution functions between surface cations and anions and water adsorbates on the A- and B-terminations.

3.1.1 A-Termination

32 potential adsorption sites are present on this surface: the cobalt and iron ions in the octahedral voids (16) and the 8 iron ions in the tetrahedral voids on which up to two molecules can adsorb. As seen from snapshots of equilibrium trajectories (Figure 3, left), both water molecules, water OH groups and surface OH arising from proton transfer are present in the contact layer.

Figure 4a shows the bond length distances between surface cations and water oxygens. While molecular water is present on all adsorption sites as exteriorised by the peaks centred at 2.15 Å, 2.25 Å and 2.35 Å for Fe^{3+}(tet), Co^{2+}(oct) and Fe^{3+}(oct), respectively. It is seen that hydroxides bind preferentially on Co^{2+}(oct) and Fe^{3+}(tet) with a stronger signature on the latter sites as can be shown by the intensity of the peaks centred at 1.9 Å and 1.95 Å, respectively. Hydroxides are barely present on the Fe^{3+}(oct) sites as seen from the broad peak of very low amplitude centred at 2.20 Å.

Our investigations reveal that about 21 (21.4) adsorbates are present in the contact layer with the surface, 7.1 hydroxides and 14.3 water molecules. The distribution of adsorbates on the adsorption sites reads: 8.8 molecules on Fe^{3+}(tet), 7.5 and 5.1 on Fe^{3+}(oct) and Co^{3+}(oct), respectively. 5.4 out of 7.1 hydroxides bind on Fe^{3+}(tet) which confirms the stronger preference of water

Preprints (www.preprints.org) | NOT PEER-REVIEWED | Posted: 2 August 2022 doi:10.20944/preprints202208.0049.v1

to dissociate on these sites as mentioned above.

Figure 4b shows the radial distribution function of the different surface oxygen types to the water hydrogens. One can see a signature of H-bonding between the surface O1 and water hydrogens as highlighted by the peak at 1.8 Å. The characteristic peaks at 1 Å shows a more significant presence of hydrogens bound to the O1 surface oxygens compared to O2 surface oxygens. This stems from the fact that proton transfer on the latter occurs only upon reconstruction of some of the nearby Fe^{3+}(tet) that move away from the tetrahedral voids, annihilating the steric effets that prohibit proton transfer to surface O2 oxygens.

3.1.2 B-Termination

In the case of the B-terminated surface, 16 potential adsorption sites are present, which are the 8 Co^{2+}(oct) and 8 Fe^{3+}(oct). On each site, only one water or hydroxide molecule can adsorb. Unlike on the A-termination, water seats on all adsorption sites. As seen from Figure 3 (right) water adsorbs via a partly dissociative mode, with a lower dissociation degree compared to the A-termination. Figure 5a shows the radial distribution function between surface cations and water oxygens. Hydroxide molecules almost exclusively bind on Fe^{3+}(oct) sites. This is supported by the peak centred at 1.95 Å, characteristic signature of OH groups which is quenched for Co^{2+}(oct) which interact exclusively with molecular water.

The integration of the number density shows that 3.1 water molecules out of the 16 present in the contact layer dissociate via proton transfer to the surface. This occurs exclusively on surface oxygens O2 as it is from Figure 5b in which the characteristic peak at 1.05 Å, signature of surface OH originating from proton transfer to the surface is missing for surface oxygens O1. Also, these surface oxygens O2 are predominant in the hydrogen bonding to the surface as can be seen from the peak centred at 1.75 Å which also exteriorises a strong H-bonding character.

Preprints (www.preprints.org) | NOT PEER-REVIEWED | Posted: 2 August 2022 doi:10.20944/preprints202208.0049.v1

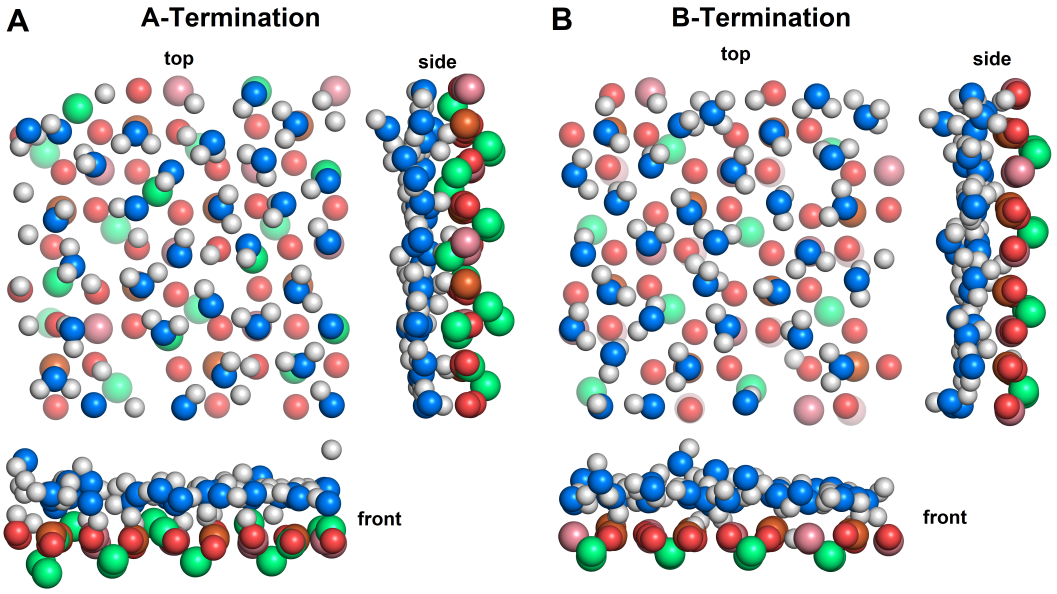

Figure 3: Snapshots of final configurations of each simulation. Fe^{3+}(tet) : green, Fe^{3+}(oct): brown, Co^{2+}(oct) : purple, slab oxygens: red, water/hydroxide oxygen: blue, hydrogen: white. Greyed-out atoms are located in lower layers.

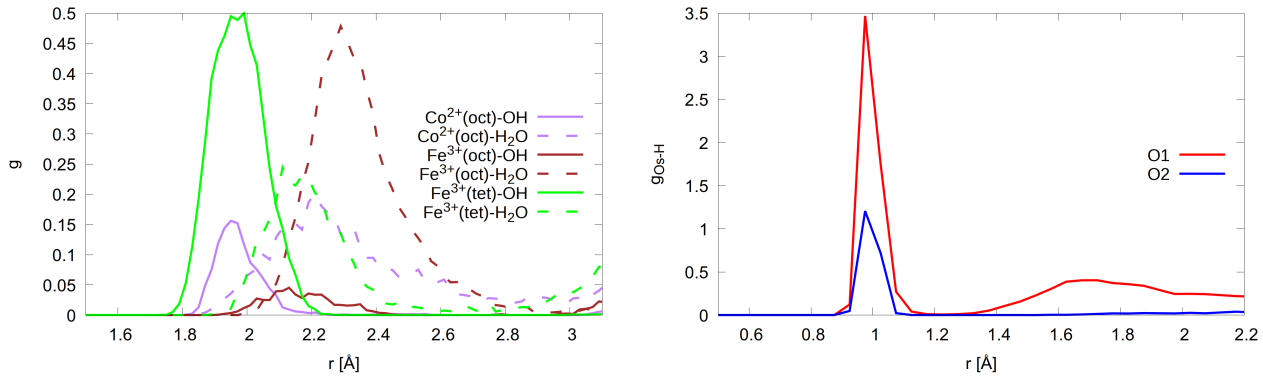

(a) (b)

Figure 4: Radial distribution function of the adsorptions sites to the oxygen of water and hydroxide molecules (a) and the radial distribution Function of the two lattice oxygen types (O1, O2) to hydrogen, A-termination.

Preprints (www.preprints.org) | NOT PEER-REVIEWED | Posted: 2 August 2022 doi:10.20944/preprints202208.0049.v1

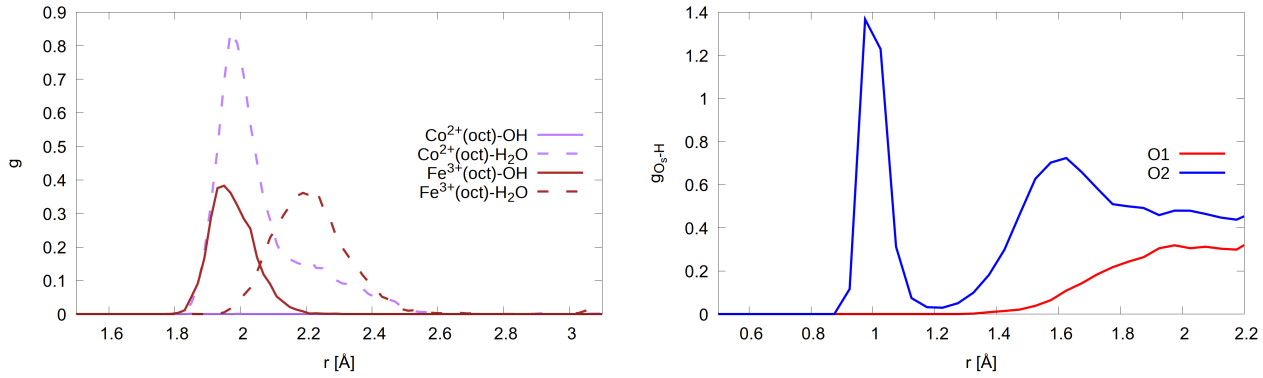

(a) (b)

Figure 5: Radial distribution function of the adsorptions sites to the oxygen of water and hydroxide molecules (a) and the radial distribution function of the two lattice oxygen types (O1, O2) to hydrogen, B-termination.

3.2 Surface relaxations and reconstructions

To study the structural behaviour of the A- and B- surfaces terminations upon water adsorption, for each surface termination, we performed molecular dynamics runs at room temperature for simulations times of 20 ps for the water free and water covered surfaces, respectively. Afterwards, we computed and analyzed characteristic density profiles and radial distribution functions (RDFs) to investigate the changes in the geometrical features before and after the simulations taking the clean surfaces as references.

3.2.1 A-Termination

After relaxation of the water free surface, the tetrahedral voids containing the Fe^{3+}(tet) are widened (6 out of 8 Fe^{3+}(tet) in the top most layer L0) as these ions move towards the nearby unoccupied octahedral voids in L1(Figure 6a,c). This is supported by Figure 7a that shows the distances between Fe^{3+}(tet) in L0 and L2 and the surface O of the tetrahedral voids located in the adjacent layers L1 and L3, respectively. For the clean surface, Fe^{3+}(tet) in L0 are displaced by about 0.05 Å from their bulk positions as shown by the peak at 1.95 Å. Besides, the broader peak's shoulder of lower amplitude at 2.2

Preprints (www.preprints.org) | NOT PEER-REVIEWED | Posted: 2 August 2022 doi:10.20944/preprints202208.0049.v1

Å, arises as the Fe^{3+}(tet) move closer to the surface oxygens located in the unoccupied octahedral voids in L1. These Fe^{3+}(tet) in L0 weakly interact with the lattice oxygens located in the unoccupied octahedral void in L3 as illustrated by the peak 2.8 Å. The presence of water slightly attenuate these relaxation features(Figure 6b,d) as illustrated by the lower amplitude of the RDFs (blue lines in Figure 7a). The Fe^{3+}(tet) in the inner layer L2 show also this tendency to move towards the octahedral voids, but the effect is not as pronounced as in the topmost layer L0 as shown by the faster convergence of the radial distribution functions towards bulk values in dry and humid conditions(dashed lines in Figure 7a) . Only 2 out of 8 Fe^{3+}(tet) reconstruct in L2.

The reconstruction of Fe^{3+}(tet), as they move towards the nearby unoccupied octahedral voids yields an increment in the coordination number in the outermost surface layers. The calculated coordination numbers for the clean surface read 4.87, 4.50 and 4.01 for Fe^{3+}(tet) in layers L0, L2 and L4 respectively. As a consequence of water adsorption, the coordination number of Fe^{3+}(tet) in the contact layer with water increases to 5.45, while the coordination environment of Fe^{3+}(tet) in inner layers remains almost inchanged with coordination numbers of 4.45 and 4.01 for Fe^{3+}(tet) in layers L2 and L4. The out of plane distribution of Fe^{3+}(tet) displayed in Figure 7b shows that the outermost Fe^{3+}(tet) undergo an inwards relaxation, moving closer to L1 as illustrated by the shift by about 0.5 Å to lower values from the bulk positions. The peak intensity is attenuated by water adsorption and spreads till bulk positions as the coordination environment of Fe^{3+}(tet) ions changes as mentioned above.

As a consequence of the clean surface reconstruction, octahedral voids containing the Co^{3+}(oct) shrink (Figure 6a,c) as supported by Co^{3+}(oct)-Os distances that shift to lower value by about 0.5 Å compared to bulk (Figure 7c). Fe^{3+}(oct) undergo relaxations of small amplitude as it can be seen from (Figure 7e). Upon water adsorption the voids are enlarged as illustrated by larger Fe^{3+}(oct)-Os distances. Co^{3+}(oct) and Fe^{3+}(oct) undergo inwards and outwards out of plane relaxation of very weak amplitude as shown in Figure 7d and Figure 7f, respectively. This observation also holds in the presence

Preprints (www.preprints.org) | NOT PEER-REVIEWED | Posted: 2 August 2022 doi:10.20944/preprints202208.0049.v1

of water as the density profiles are very similar. Water adsorption yields a bulk like coordination environment (5.86 and 5.6 for Fe^{3+}(oct) and Co^{3+}(oct), respectively vs. 6 for the bulk coordination number).

3.2.2 B-Termination

Fe^{3+}(tet) located in L2 reconstruct on the clean surface (3 out of 8 Fe^{3+}(tet)), by moving into unoccupied octahedral voids in L1 (Figure 8a,c) as is highlighted by the tail in the RDF (Figure 9a) and the presence of the peak at -0.1 Å in their density profiles which expressses an outwards relaxation by about 0.9 Å(Figure 9b). This increases the coordination number of outermost Fe^{3+}(tet) to 4.38. Their counterparts in the inner layers L4 and L6 do not reconstruct and their coordination numbers barely deviate from bulk values (4.03 and 4.07 respectively). Upon water adsorption, the reconstruction in L2 is lifted as the presence of water quenches the above mentioned geometric features. As a consequence, the Fe^{3+}(tet) in L2 recover their bulk environment with a coordination number of 4.02.

Like on the A-termination, a consequence of the Fe^{3+}(tet) reconstruction is the shrinking of the octahedral voids containing the Co^{3+}(oct) that can be observed in L1 layer (Figure 8a,c). The shortening of the Co^{3+}(oct)-Os distances as shown in Figure 9c supports this observation. This holds in dry and humid conditions(Figure 8b,d). Figure 9d shows that the Co^{3+}(oct) undergo almost no out of plane relaxation. This is a consequence of the weaker interaction of Co^{3+}(oct) with water as shown in Figure 5a and discussed above. Water enlarges the octahedral voids containing the Fe^{3+}(oct) as it can be seen from the broadening of the RDF of the outermost Fe^{3+}(oct) in Figure 9e and their outwards out-of-plane relaxation in Figure 9f. This stems from their stronger interaction with water hydroxide. Also, like the Fe^{3+}(tet), upon water adsorption, the 5-fold coordinated Fe^{3+}(oct) and Co^{3+}(oct) recover their bulk coordination number of 6.

Preprints (www.preprints.org) | NOT PEER-REVIEWED | Posted: 2 August 2022 doi:10.20944/preprints202208.0049.v1

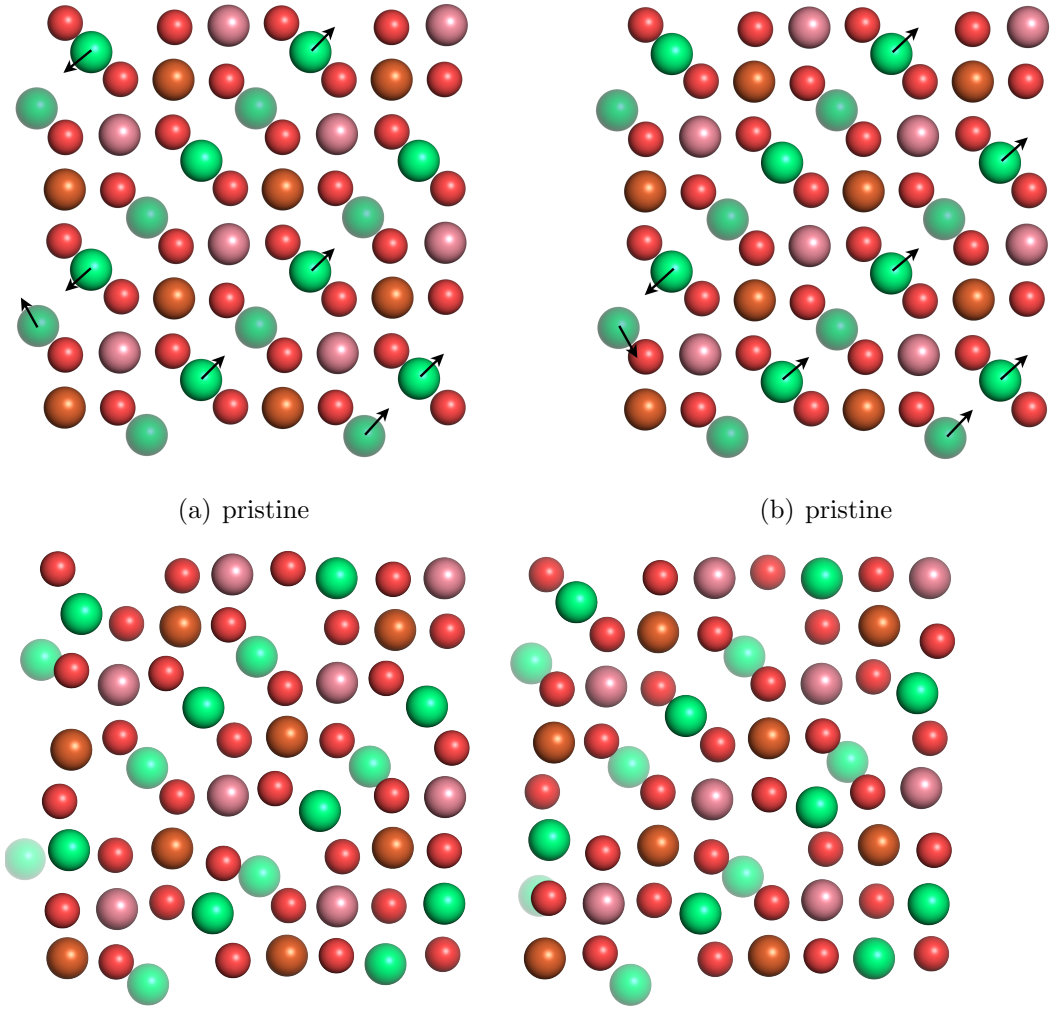

(a) pristine (b) pristine

(c) vacuum (d) water

Figure 6: Top views of the initial (top row) and final (after 20 ps; bottom row) surface structures for A-terminated water-free (left) and water covered (right) $CoFe_2O_4$ (001) surfaces, with atom colouring Fe^{3+}(oct): brown, Fe^{3+}(tet): green, Co^{3+}: purple, O: red as in Fig. 2. Fe^{3+}(tet) ions below the top surface layers are partially greyed out. The arrows indicate the reconstruction of the Fe^{3+}(tet)

.

Preprints (www.preprints.org) | NOT PEER-REVIEWED | Posted: 2 August 2022 doi:10.20944/preprints202208.0049.v1

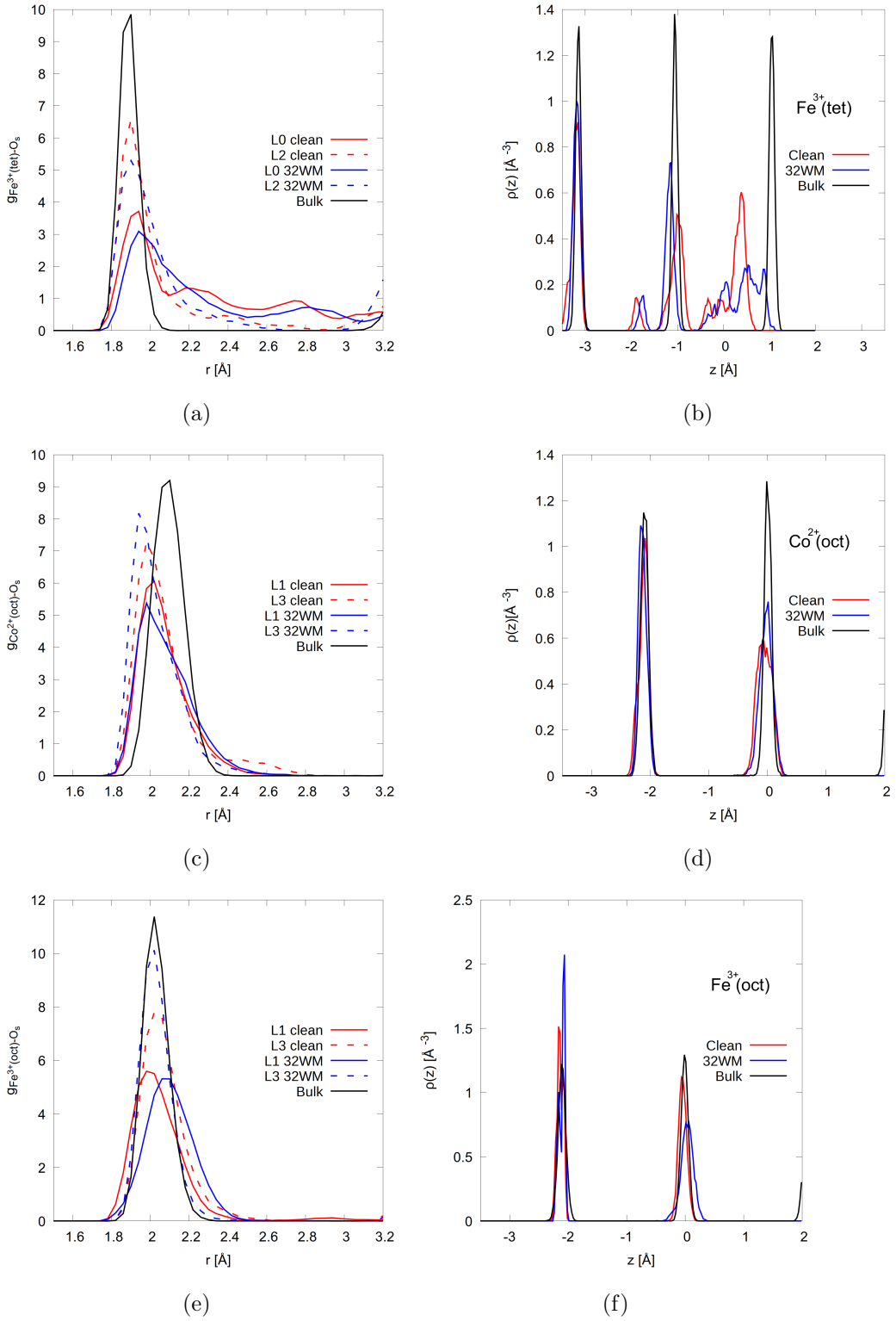

Figure 7: radial distribution function (left) of the lattice oxygens to cobalt and iron ions in the 4 outermost layers (L0-L3) and density profiles (right) of the latter on the A-terminated surface. The center of mass of layer L1 (see Figure 1) is taken as reference position z=0.

.

Preprints (www.preprints.org) | NOT PEER-REVIEWED | Posted: 2 August 2022 doi:10.20944/preprints202208.0049.v1

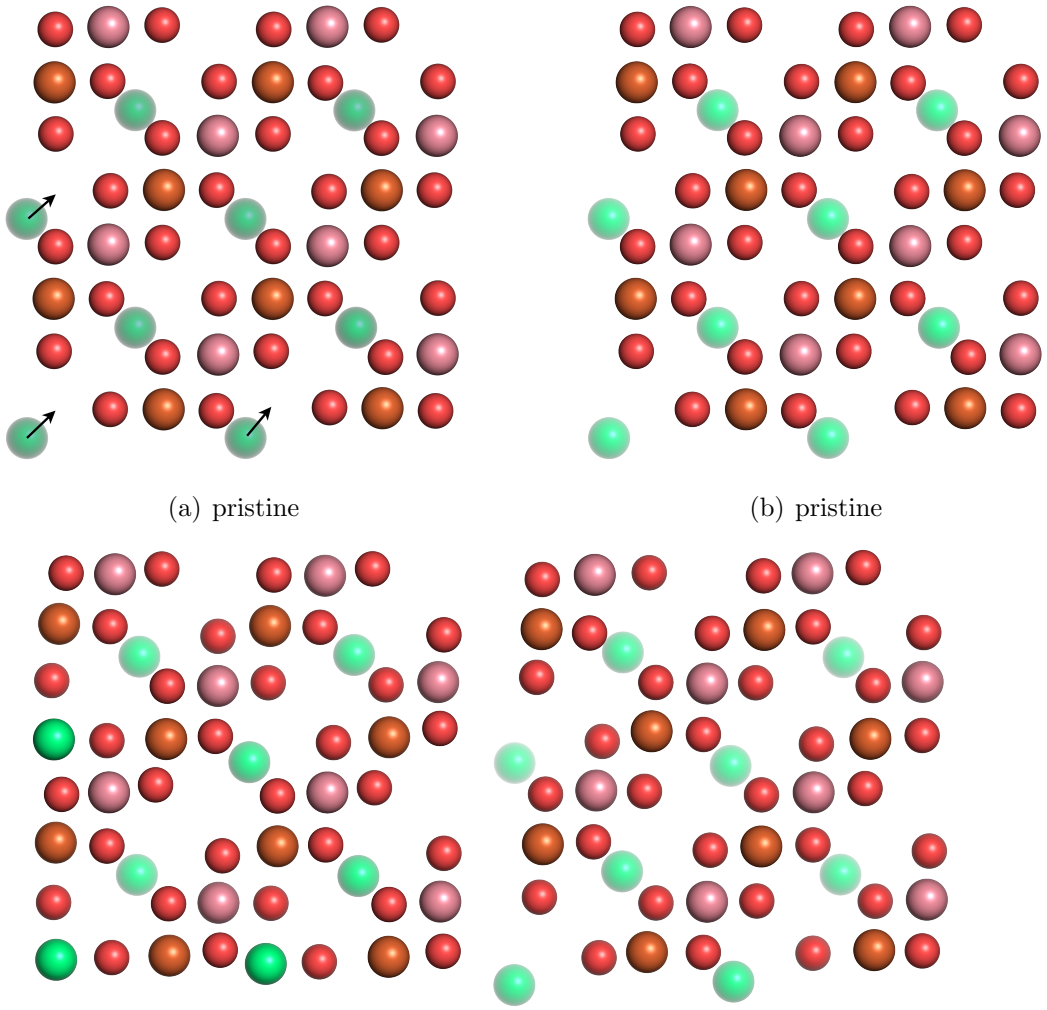

(a) pristine (b) pristine

(c) vacuum (d) water

Figure 8: Top views of the initial (top row) and final (after 10 ps; bottom row) surface structures for B-terminated water-free (left) and water covered (right) $CoFe_2O_4$ (001) surfaces, with atom colouring Fe^{3+}(oct): brown, Fe^{3+}(tet): green, Co^{3+}: purple, O: red as in Fig. 2. Fe^{3+}(tet) ions below the top surface layers are partially greyed out. The arrows indicate the reconstruction of the Fe^{3+}(tet)

.

Preprints (www.preprints.org) | NOT PEER-REVIEWED | Posted: 2 August 2022 doi:10.20944/preprints202208.0049.v1

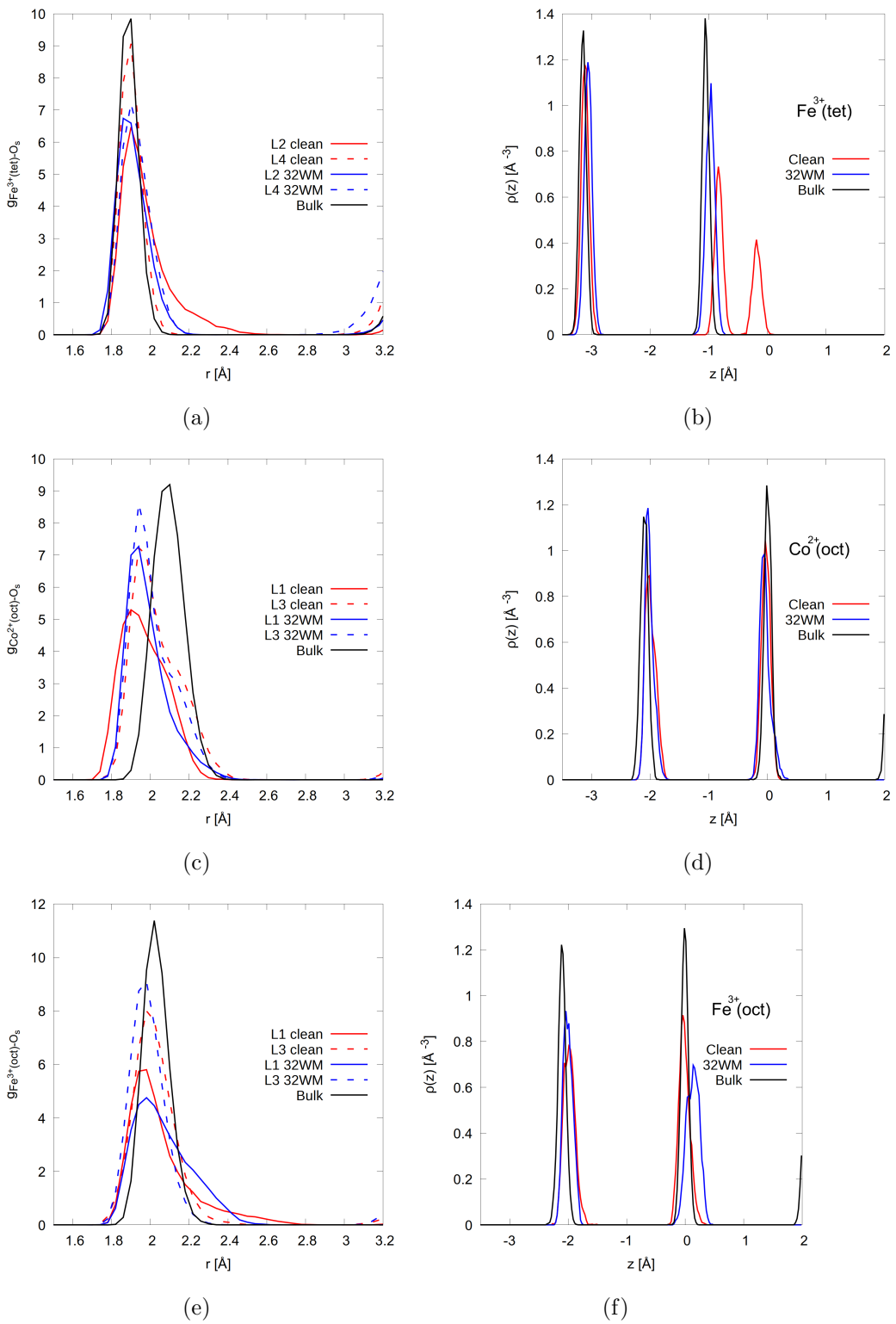

Figure 9: radial distribution function (left) of the lattice oxygens to the cobalt and iron ions in the 4 layers outermost (L1-L4) and density profiles (right) of the latter on the B-terminated surface. The center of mass of layer L1 (see Figure 1) is taken as reference position z=0.

 doi:10.20944/preprints202208.0049.v1

4 Conclusion

Our investigations have shown that on both the A- and B-terminations water is partially dissociated in the contact layer. Molecular water can bind on all cation sites, while hydroxide binds to specific sites. On the A-terminated surface, hydroxide molecules mainly bind on the 2-fold coordinated iron ions Fe^{3+}(tet), while on the B-terminated surface, they sit exclusively ontop the 5-fold coordinated iron ions Fe^{3+}(oct) which are more reactive. The dissociation degree on the A-terminated surface is higher than on the B-termination (A: 7/24, 30% B:3/16, 19%). Following water dissociation, proton transfer to a nearby surface oxygen occurs, resulting in a surface hydroxide. On the A-termination, proton transfer to the surface oxygens O1 in the topmost layer (L1) that are coordinated to one Fe^{3+}(tet) in the adjacent subsurface layer L2 is more pronounced while on the B-termination it occurs exclusively on the O2 surface oxygens in the layer L1. Both surface terminations undergo reconstruction in dry conditions. The Fe^{3+}(tet) in the top most layer L0 on the A-termination and those in L2 on the B-termination move towards the nearby unoccupied octahedral voids in layer L1. Water partially lifts the reconstructions on the A- termination and does it completely on the B-termination as on the latter the undercoordinated surface atoms converge more faster to their bulk-like environment in presence of a thin film of 32 water molecules.

Acknowledgments

This study was funded by the Deutsche Forschungsgemeinschaft (DFG, German Research Foundation) – 388390466 – TRR 247 within the work of Project A6. The authors gratefully acknowledge computing time granted by the Center for Computational Sciences and Simulation (CCSS) of the Universität of Duisburg-Essen and provided on the supercomputer magnitUDE (DFG grants INST 20876/209-1 FUGG, INST 20876/243-1 FUGG) at the Zentrum für Informations- und Mediendienste (ZIM).

 doi:10.20944/preprints202208.0049.v1

References

[1] Qing Zhao, Zhenhua Yan, Chengcheng Chen, and Jun Chen. Spinels: Controlled preparation, oxygen reduction/evolution reaction application, and beyond. *Chemical Reviews*, 117(15):10121–10211, 2017. PMID: 28745484.

[2] EJW Verwey and EL Heilmann. Physical properties and cation arrangement of oxides with spinel structures i. cation arrangement in spinels. *The Journal of Chemical Physics*, 15(4):174–180, 1947.

[3] Charles Guillaud. Propriétés magnétiques des ferrites. *Journal de Physique et le Radium*, 12(3):239–248, 1951.

[4] Daniel Fritsch and Claude Ederer. Epitaxial strain effects in the spinel ferrites cofe 2 o 4 and nife 2 o 4 from first principles. *Physical review B*, 82(10):104117, 2010.

[5] Kalapu Chakrapani, Georg Bendt, Hamidreza Hajiyani, Ingo Schwarzrock, Thomas Lunkenbein, Soma Salamon, Joachim Landers, Heiko Wende, Robert Schlögl, Rossitza Pentcheva, Malte Behrens, and Stephan Schulz. Role of composition and size of cobalt ferrite nanocrystals in the oxygen evolution reaction. *ChemCatChem*, 9(15):2988–2995, 2017.

[6] Kalapu Chakrapani, Georg Bendt, Hamidreza Hajiyani, Thomas Lunkenbein, Mark T. Greiner, Liudmyla Masliuk, Soma Salamon, Joachim Landers, Robert Schlögl, Heiko Wende, Rossitza Pentcheva, Stephan Schulz, and Malte Behrens. The role of composition of uniform and highly dispersed cobalt vanadium iron spinel nanocrystals for oxygen electrocatalysis. *ACS Catalysis*, 8(2):1259–1267, 2018.

[7] Yu Xu, Fatih Özcan, Philipp Zielke, Stefanie Becker, Manuel Heimann, Justus Heese, Kalapu Chakrapani, Malte Behrens, Søren Bredmose Simonsen, Poul Norby, et al. Continuous hydrothermal flow synthesis of co1–xnixfe2o4 (x= 0–0.8) nanoparticles and their catalytic properties for co oxidation and oxygen evolution reaction. *Zeitschrift für anorganische und allgemeine Chemie*, 644(24):1727–1733, 2018.

[8] Abdelilah El Arrassi, Zhibin Liu, Mathies V Evers, Niclas Blanc, Georg Bendt, Sascha Saddeler, David Tetzlaff, Darius Pohl, Christine Damm, Stephan Schulz, et al. Intrinsic activity of oxygen evolution catalysts probed at single cofe2o4 nanoparticles. *Journal of the American Chemical Society*, 141(23):9197–9201, 2019.

[9] Gary Evans, Ivan V Kozhevnikov, Elena F Kozhevnikova, John B Claridge, Ramanathan Vaidhyanathan, Calum Dickinson, Colin D Wood, Andrew I Cooper, and Matthew J Rosseinsky. Particle size–activity relationship for cofe 2 o 4 nanoparticleco oxidation catalysts. *Journal of Materials Chemistry*, 18(45):5518–5523, 2008.

[10] P. Mountapmbeme Kouotou, H. Vieker, Z. Y. Tian, P. H. Tchoua Ngamou, A. El Kasmi, A. Beyer, A. Gölzhäuser, and K. Kohse-Höinghaus. Structure–activity relation of spinel-type co–fe oxides for low-temperature co oxidation. *Catalysis Science & Technology*, 4(9):3359–3367, 2014.

[11] Dong Gu, Chun-Jiang Jia, Claudia Weidenthaler, Hans-Josef Bongard, Bernd Spliethoff, Wolfgang Schmidt, and Ferdi Schueth. Highly ordered mesoporous cobalt-containing oxides: structure, catalytic properties, and active sites in oxidation of carbon monoxide. *Journal of the American Chemical Society*, 137(35):11407–11418, 2015.

[12] Jasmine Thomas, Nygil Thomas, Frank Girgsdies, Malte Beherns, Xing Huang, VD Sudheesh, and Varkey Sebastian. Synthesis of cobalt ferrite nanoparticles by constant ph co-precipitation and their high catalytic activity in co oxidation. *New Journal of Chemistry*, 41(15):7356–7363, 2017.

[13] Sven Anke, Tobias Falk, Georg Bendt, Ilya Sinev, Michael Haevecker, Hendrik Antoni, Ioannis Zegkinoglou, Hyosang Jeon, Axel Knop-Gericke, Robert Schlögl, et al. On the reversible deactivation of cobalt ferrite spinel nanoparticles applied in selective 2-propanol oxidation. *Journal of Catalysis*, 382:57–68, 2020.

[14] Tobias Falk, Eko Budiyanto, Maik Dreyer, Christin Pflieger, Daniel Waffel, Julia Büker, Claudia Weidenthaler, Klaus Friedel Ortega, Malte Behrens, Harun Tüysüz, et al. Identification of active sites in the catalytic oxidation of 2-propanol over co1+ xfe2–xo4 spinel oxides at solid/liquid and solid/gas interfaces. *ChemCatChem*, 2021.

[15] M Kooti and M Afshari. Magnetic cobalt ferrite nanoparticles as an efficient catalyst for oxidation of alkenes. *Scientia Iranica*, 19(6):1991–1995, 2012.

[16] Raluca Dumitru, Florica Papa, Ioan Balint, Daniela C Culita, Cornel Munteanu, Nicolae Stanica, Adelina Ianculescu, Lucian Diamandescu, and Oana Carp. Mesoporous cobalt ferrite: A rival of platinum catalyst in methane combustion reaction. *Applied Catalysis A: General*, 467:178–186, 2013.

[17] Claudia Maria Simonescu, Alina Tătăruş, Daniela Cristina CuliŢă, Nicolae Stănică, Ioana Alexandra Ionescu, Bogdan Butoi, and Ana-Maria Banici. Comparative study of cofe(2)o(4) nanoparticles and cofe(2)o(4)-chitosan composite for congo red and methyl orange removal by adsorption. *Nanomaterials (Basel, Switzerland)*, 11, Mar 2021.

[18] Haimei Zheng, Qian Zhan, Florin Zavaliche, Matt Sherburne, Florian Straub, Maria P. Cruz, Long-Qing Chen, Uli Dahmen, and R. Ramesh. Controlling Self-Assembled PerovskiteSpinel Nanostructures. 7 2006.

[19] Xi'an Fan, Jianguo Guan, Xiaofen Cao, Wei Wang, and Fangzhi Mou. Low-temperature synthesis, magnetic and microwave electromagnetic properties of substoichiometric spinel cobalt ferrite octahedra. *European Journal of Inorganic Chemistry*, 2010(3):419–426, 2010.

[20] Stephane Kenmoe and P. Ulrich Biedermann. Water adsorbate phases on zno and impact of vapor pressure on the equilibrium shape of nanoparticles. *The Journal of Chemical Physics*, 148(5):054701, 2018.

[21] Hamidreza Hajiyani and Rossitza Pentcheva. Surface termination and composition control of activity of the coxni1–xfe2o4(001) surface for water oxidation: Insights from dft+u calculations. *ACS Catalysis*, 8(12):11773–11782, 2018.

[22] Le T. Lu, Ngo T. Dung, Le D. Tung, Cao T. Thanh, Ong K. Quy, Nguyen V. Chuc, Shinya Maenosono, and Nguyen T. K. Thanh. Synthesis of magnetic cobalt ferrite nanoparticles with controlled morphology, monodispersity and composition: the influence of solvent, surfactant, reductant and synthetic conditions. *Nanoscale*, 7:19596–19610, 2015.

[23] Yunji Eom, Mohamed Abbas, HeeYoon Noh, and CheolGi Kim. Morphology-controlled synthesis of highly crystalline fe3o4 and cofe2o4 nanoparticles using a facile thermal decomposition method. *RSC Adv.*, 6:15861–15867, 2016.

[24] Arjeta Rushiti, Christof Hättig, Bo Wen, and Annabella Selloni. Structure and reactivity of pristine and reduced spinel cofe2o4 (001)/(100) surfaces. *The Journal of Physical Chemistry C*, 125(18):9774–9781, 2021.

[25] Stephane Kenmoe and P. Ulrich Biedermann. Water aggregation and dissociation on the zno(100) surface. *Phys. Chem. Chem. Phys.*, 19:1466–1486, 2017.

[26] T. Kox, E. Spohr, and S. Kenmoe. Impact of solvation on the structure and reactivity of the co3o4 (001)/h2o interface: Insights from molecular dynamics simulations. *Frontiers in Energy Research*, 8:312, 2020.

[27] Stephane Kenmoe, Oleg Lisovski, Sergei Piskunov, Dmitry Bocharov, Yuri F. Zhukovskii, and Eckhard Spohr. Water adsorption on clean and defective anatase tio2 (001) nanotube surfaces: A surface science approach. *The Journal of Physical Chemistry B*, 122(21):5432–5440, 2018. PMID: 29596747.

[28] S. Kenmoe, O. Lisovski, S. Piskunov, Y. F. Zhukovskii, and E. Spohr. Electronic and optical properties of pristine, n- and s-doped water-covered tio2 nanotube surfaces. *The Journal of Chemical Physics*, 150(4):041714, 2019.

[29] The CP2K developers group. CP2K is freely available from: http://www.cp2k.org/, 2016.

[30] John P. Perdew, Kieron Burke, and Matthias Ernzerhof. Generalized gradient approximation made simple. *Phys. Rev. Lett.*, 77:3865–3868, Oct 1996.

[31] Stefan Grimme, Jens Antony, Stephan Ehrlich, and Helge Krieg. A consistent and accurate ab initio parametrization of density functional dispersion correction (DFT-D) for the 94 elements H-Pu. *The Journal of Chemical Physics*, 132(15):154104, 2010.

[32] J. Hubbard and Brian Hilton Flowers. Electron correlations in narrow energy bands. *Proceedings of the Royal Society of London. Series A. Mathematical and Physical Sciences*, 276(1365):238–257, 1963.

[33] Abraham Atour Zigla, Tim Kox, Daniel Mevoa, Hypolite Todou Assaouka, Issah Njiawouo Nsangou, Daniel Manhouli Daawe, Stephane Kenmoe, and Patrick Mountapmbeme Kouotou. Magnesium-modified co3o4 catalyst with remarkable performance for toluene low temperature deep oxidation. *Catalysts*, 12(4), 2022.

[34] Swen Zerebecki, Soma Salamon, Joachim Landers, Yuke Yang, Yujin Tong, Eko Budiyanto, Daniel Waffel, Maik Dreyer, Sascha Saddeler, Tim Kox, Stephane Kenmoe, Eckhard Spohr, Stephan Schulz, Malte Behrens, Martin Muhler, Harun Tüysüz, R. Kramer Campen, Heiko Wende, Sven Reichenberger, and Stephan Barcikowski. Engineering of cation occupancy of cofe2o4 oxidation catalysts by nanosecond, single-pulse laser excitation in water. *ChemCatChem*, 14(10):e202101785, 2022.

 doi:10.20944/preprints202208.0049.v1

[35] Eko Budiyanto, Swen Zerebecki, Claudia Weidenthaler, Tim Kox, Stephane Kenmoe, Eckhard Spohr, Serena DeBeer, Olaf Rüdiger, Sven Reichenberger, Stephan Barcikowski, and Harun Tüysüz. Impact of single-pulse, low-intensity laser post-processing on structure and activity of mesostructured cobalt oxide for the oxygen evolution reaction. *ACS Applied Materials & Interfaces*, 13(44):51962–51973, 2021. PMID: 34323466.

[36] Kanchan Ulman, Emiliano Poli, Nicola Seriani, Simone Piccinin, and Ralph Gebauer. Understanding the electrochemical double layer at the hematite/water interface: A first principles molecular dynamics study. *The Journal of chemical physics*, 150(4):041707, 2019.